EARTH OBSERVATION AND GEOMATICS ENGINEERING
website: https://eoge.ut.ac.ir

Evaluating an S-band ground-based synthetic aperture radar imaging system for LFMCW SAR processing

Benyamin Hosseiny, Jalal Amini*, Majid Esmaeilzadeh, Mehran Nekoee

School of Surveying and Geospatial Engineering, College of Engineering, University of Tehran, Tehran, Iran

Article history:
Received: 11 July 2020, Received in revised form: 10 January 2021, Accepted: 15 January 2021

ABSTRACT

Ground-based synthetic aperture radar (GBSAR) imaging systems are used extensively in earth observation and remote sensing applications. They are lightweight, cost efficient, and resolve the main limitations of airborne and spaceborne SAR systems, such as low data collection rate, complicated implantation, and inefficient viewing angle to the imaging scene. This paper evaluates the signal processing results of the developed and implemented GBSAR system at the microwave remote sensing laboratory (MRESL) of the University of Tehran. The radar sensor consists of linear frequency modulated continuous wave (LFMCW) operating in S band with 330 MHz of bandwidth that is mounted on a 1.4 m linear rail with a stepper motor. The radar sensor moves every 1 cm and records the backscattered echoes. After the dechirping process and digitizing, the recorded signal is stored in a two dimensional array, known as SAR 2D raw matrix. Experiments were conducted by illuminating the SAR sensor toward a scene containing corner reflectors. SAR raw data were processed by implementing the back projection algorithm, and results were evaluated and compared with numerical simulations. Furthermore, the Hann window was employed as a weighting function on the raw signal, and its effect was evaluated on the resulting SAR image. The obtained results are promising and show the effectiveness of the developed GBSAR in the discrimination of targets at two range and cross-range directions.

KEYWORDS

GBSAR
SAR signal processing
Backprojection
Imaging
Window function.

1. Introduction

Synthetic aperture radar (SAR) is widely used in earth observation and has made significant progress in solving remote sensing problems. The main feature of SAR systems is that they operate in the microwave band of the electromagnetic spectrum, which can collect data at night and in any weather conditions (Bamler & Hartl, 1998; Massonnet & Feigl, 1998). In the past two decades, the implementation and development of ground-based synthetic aperture radar (GBSAR) have significantly impacted the applications of remote sensing of the environment. This system includes a radar sensor that sends and receives electromagnetic waves and repeats this operation as it travels on a rail with a specific length (Bernardini, Ricci, Coppi, & others, 2007; Hanssen, 2001). Rail's length is the main factor in improving the cross-range resolution, where increasing the rail's length results in a narrower synthetic aperture beamwidth and hence a better resolution (Carrara, Goodman, & Majewski, 1995).

Most remote sensing radar sensors, such as those mounted on satellites or airplanes, perform based on pulse signals. Pulsed radars mostly have a very short duration, which needs high voltage power to propagate in space and making a strong backscatter from a target (Richards, Scheer,

* Corresponding author
E-mail addresses: ben.hosseiny@ut.ac.ir (B. Hosseiny); jamini@ut.ac.ir (J. Amini); m.esmaeilzade@ut.ac.ir (M. Esmaeilzade); mehran.nekoee@ut.ac.ir (M. Nekoee);
DOI: 10.22059/eoge.2021.306032.1084

Published online: 21 January 2021

Holm, & Melvin, 2010). However, GBSAR, as a low-power system, mostly uses frequency modulated continuous wave (FMCW) signal (Charvat, 2014). FMCW signal can increase the signal power by continuous signal generation. Therefore, the need for a high-power signal generator is decreased, which significantly reduces the manufacturing cost. Also, by frequency modulating the signal, we can increase the signal bandwidth without reducing the signal pulse duration, which leads to higher resolution with high pulse duration (Skolnik, 2003). Accordingly, low-cost, lightweight, and high data acquisition rates make GBSAR an attractive system for solving remote sensing problems.

In the past two decades, GBSAR systems have been tested and employed in various earth observation researches. These applications cover a wide range of landslide displacement or rock drift, rock slope surveillance, surface collapse monitoring, and surface changes of glaciers and snowy areas. Tarchi et al. (1999) and Alba et al. (2008) used GBSAR for dam monitoring. Del Ventisette et al. (2011) used Ku-band GBSAR for continuous monitoring of landslides. Other studies used GBSAR for structural health monitoring (Pieraccini, 2013; Pieraccini & Miccinesi, 2019). Several studies also used GBSAR to monitor volcanos. For instance, Casagli et al. (2010) used GBSAR as a warning system for the Stromboli volcano while monitoring and measuring changes resulting from this volcano eruption. Dammann et al. (2020) employed a Ku-band interferometric GBSAR with a vertical synthetic aperture to monitor sea ice movements.

The above-mentioned GBSAR systems utilize high-frequency radar sensors that are most suitable for displacement monitoring. However, using a low-frequency radar, a wide range of applications, including moisture retrieval and volumetric scattering, can be enabled by GBSAR systems (Anghel et al., 2019; Ulaby et al., 2014). Martinez and Fortney (2007) employed a C-band GBSAR for monitoring Snow for classification and detection of avalanches. Similarly, Schaffhauser et al. (2008), in a study, used a C-band GBSAR for retrieving the snow depth and water content. A tomographic L-band GBSAR was developed by Penner and Long (2017) for 3D and volumetric imaging of trees.

As a summary, most of the GBSAR systems use high-frequency radars, which are useful for displacement monitoring, but the applications and development of low-frequency GBSAR systems for remote sensing of targets' parameters may be overlooked, and it is gaining attention in recent literature (Anghel et al., 2019). Therefore, the main objective of this paper is to demonstrate the established signal processing experiments for the development of a GBSAR imaging system. The SAR raw data is acquired by S-band FMCW GBSAR, developed and implemented at the microwave remote sensing laboratory (MRESL) of the University of Tehran[2]. Before moving to the applications of a developed system, it is essential to become sure about its performance and evaluate its parameters in simulation or real-world scenarios (Hosseiny & Amini, 2018). Accordingly, this paper aims to assess the recorded radar echo and its corresponding signal processing steps for obtaining the final SAR image by numerical simulations and real data acquired in the lab.

2. Theoretical Background

SAR processing is divided into two main steps: range processing and cross-range processing. Figure 1 shows the processing chain of SAR processing for generating a focused image out of the recorded backscattered echoes. A detailed explanation of each step is provided in the following subsections.

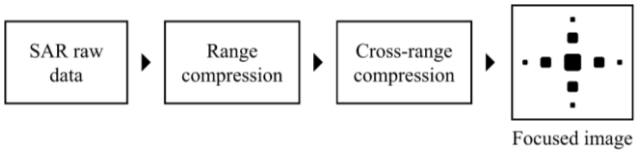

Figure 1. SAR signal processing steps

2.1. Data acquisition and preprocessing

Equation (1) shows the relation between range resolution and signal bandwidth. In simple sinusoidal pulse systems (without modulation), the signal bandwidth is equal to the inverse of pulse duration ($B = 1/\tau$). Where ρ_r is the range resolution, τ and B are the signal pulse duration and bandwidth. Equation (2). shows the relation between the signal's average power and pulse duration. Where P_{av} is the average signal power, P_t is the signal peak power, Dc is the duty cycle, and T_P is the pulse repetition interval (PRI).

$$\rho_r = \frac{c}{2B} \tag{1}$$

$$P_{av} = P_t \times Dc = P_t \times \frac{\tau}{T_P} \tag{2}$$

As it can be seen from Equations (1) and (2), in simple pulse, increasing the pulse duration increases the signal power but decreases the resolution. According to Equation (1), a large bandwidth is required to increase the resolution while increasing the bandwidth depends on reducing the pulse duration. Therefore, there is a tradeoff between signal resolution and power (Skolnik, 2003).

Continuous-wave (CW) signal has the maximum value of duty-cycle (100%), which increases the signal power. However, CW radar cannot discriminate range (Ulaby et al., 2014). A popular solution is the frequency modulation of the

[2] mresl.ut.ac.ir

radar signal. Frequency modulation (FM) of the signal makes range resolution possible. In an FM radar, the signal frequency varies as a function of time, named sweep (Ulaby et al., 2014). Various modulations are possible for signal, but linear modulation is the most common approach. In linear frequency modulation (LFM), the frequency varies linearly as a function of time (Li et al., 2017). Also, by frequency modulation of the radar signal, bandwidth can be increased without depending on the pulse duration. However, wide bandwidth frequency modulation has some system design limitations and constraints (Richards et al., 2010). As a result, combining continuous wave signal with frequency modulation can increase the signal power and resolution for target detection and range estimation. Linear FMCW (LFMCW) radars are mostly used in low power and near-field systems such as UAV-based or ground-based systems (Komarov & Smolskiy, 2003; Luo et al., 2014; Ting, Oloumi, & Rambabu, 2017).

The transmitted signal in linear frequency modulated radar, for one sweep duration (τ), can be expressed as:

$$s_t = \exp(j\,2\pi f_c t + j\,\pi c_r t^2) \tag{3}$$

where f_c is the carrier frequency, $t \in [0, \tau]$, and c_r is the chirp-rate (in some literature stated as sweep-rate), which is equal to the ratio between transmitted bandwidth and sweep duration ($c_r = B/\tau$). The received signal is a delayed version of the transmitted signal:

$$s_r = \exp(j\,2\pi f_c (t - t_d) + j\,\pi c_r (t - t_d)^2) \tag{4}$$

where t_d is the time delay. The received chirp signal needs to be compressed to detect the targets and their corresponding range. Signal compression is performed by the dechirping process (Carrara et al., 1995). Dechirping is similar to matched filtering (Soumekh, 1999) and is done by mixing a replica of the transmitted signal with the received signal and lowpass filtering. Therefore, the dechirped or beat signal (in some literature stated as intermediate signal) is generated (Meta, Hoogeboom, & Ligthart, 2007):

$$s_b = \exp(j\,2\pi(c_r t_d t + f_c t_d - \frac{1}{2} c_r t_d^2)) \tag{5}$$

where s_b is the beat signal. The range can be measured from beat frequency, which is proportional to time delay ($f_b = c_r t_d$):

$$R = \frac{c f_b \tau}{2B} = \frac{c f_b}{2c_r} \tag{6}$$

where R is range. Figure 2 shows the block diagram of an FMCW radar system. The received signal is mixed with a replica of the transmitted signal, and after lowpass filtering, the dechirped signal is saved as system output. This type of radar system is named "dechirp-on-receive" (Carrara et al., 1995). The output signal is in the frequency domain, and the compressed signal can be obtained by Fourier (Charvat, 2014).

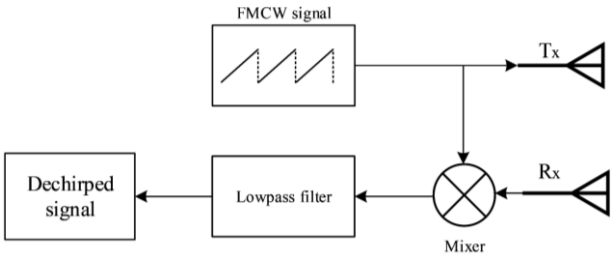

Figure 2. FMCW radar system block diagram

The maximum detectable range by radar sensor for a target with a radar cross-section (RCS) of σ is calculated based on radar equation (Skolnik, 2003):

$$R_{\max}^4 = \frac{N P_{av} G_{tx} G_{rx} \lambda_c^2 \sigma}{(4\pi)^3 k T_0 F_n B_n (Dc)(SNR)_1 L_s} \tag{7}$$

where N is the number of the integrated pulse (or number of radar steps in cross-range direction), G_{tx} and G_{rx} are transmitter and receiver antennas gain, $k = 1.38 \times 10^{-23}$ is Boltzmann's constant, $T_0 = 290K$ is standard temperature, F_n is receiver noise figure, B_n is noise bandwidth, $Dc = 1$ is FMCW signal duty cycle, $(SNR)_1$ is single pulse (sweep) signal-to-noise ratio, and L_s is system losses.

2.2. SAR cross-range processing

The main idea of synthetic aperture radar imaging is to increase radar resolution in cross-range direction by coherent integration of received signals in different cross-range positions of the radar sensor. Figure 3 shows the general SAR data acquisition geometry. SAR transmits signals periodically along with the movement of the platform along the track. Therefore, it arranges a synthetic linear array in the cross-range direction. Similar to the received signal in range direction (Equation (4)), the signal in the cross-range direction is a linear chirp as a function of cross-range steps (n). The synthetic aperture signal of step n for a scatterer located at range $R(n)$ is defined as (Zaugg & Long, 2015):

$$s_a(n) = \exp(-j\,4\pi(c_r(\frac{R(n)}{c})^2 - \frac{R(n)}{\lambda_c})) \tag{8}$$

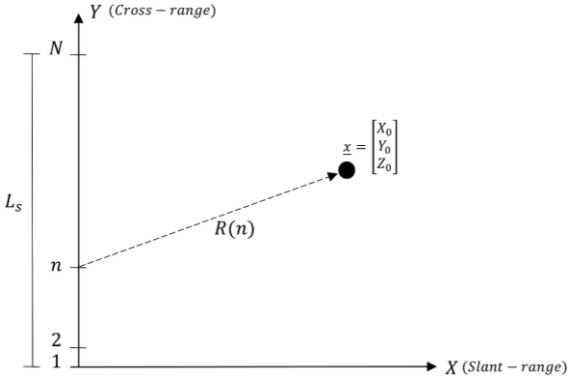

Figure 3. Synthetic aperture radar imaging geometry

A cross-range compressed signal can be obtained by the back-projection method (Zaugg & Long, 2015). After range compression, for coherent SAR processing, the cross-range phase of the 2-D signal needs to be compensated. Cross-range phase compensation is done similar to the range compression by convolving the complex conjugate of the reference cross-range signal (s_{cr}) (Yang et al., 2018). Equation (9) shows the phase compensation function for a scatterer located at $\underline{x} = (X_0, Y_0, Z_0)$ of the imaging scene. Where

$$R(\underline{x}, n) = \sqrt{(x[n]-X_0)^2 + (y[n]-Y_0)^2 + (z[n]-Z_0)^2},$$

and $x[n]$, $y[n]$, $z[n]$ are the antenna instantaneous location.

$$s_{cr}(\underline{x}, n) = \exp(j\,4\pi(c_r(\frac{R(\underline{x}, n)}{c})^2 - \frac{R(\underline{x}, n)}{\lambda_c})) \quad (9)$$

Therefore, the SAR processing chain for an FMCW system can be summarized as the following steps:

1. Radar signal dechirping by convolving a replica of the transmitted signal in a mixer and lowpass filtering
2. Range compression of dechirped signal by Fourier transform
3. Cross-range compression of SAR 2-D array by Backprojection algorithm

After Cross-range phase correction and coherent integration of SAR signals, the synthesized cross-range beamwidth (β_{cr}) for a synthetic aperture length of L_s can be defined as Equation (10). Therefore, SAR cross-range resolution (ρ_{cr}) for a scatterer with a slant range of R can be defined as Equation (11).

$$\beta_{cr} = \frac{\lambda_c}{2L_s} \quad (10)$$

$$\rho_{cr} = \beta_{cr} R = \frac{\lambda_c R}{2L_s} \quad (11)$$

2.3. Signal windowing

Window functions are generally used for decreasing the noise and increasing the quality of the signal. A window function starts near or at zero, then increases to a maximum at the center of the signal and decreases again. Window functions, in most cases, lead to suppression of the signal sidelobes. However, it has been seen that the reduction of the sidelobe level increases the bandwidth, which means decreasing the resolution in radar signal (Heinzel, Rüdiger, & Schilling, 2002; Oppenheim, 1999).

In this paper, the performance of the Hann window is investigated on the received raw signal of the GBSAR. Equation (12) shows the Hann window function for a discrete signal consisted of N samples. The Hann window has a sinusoidal shape, it starts and ends at zero, and it is a popular window function in reducing signal noises (Brooker, 2011; Podder, Khan, Khan, & Rahman, 2014).

$$W_{Hann}(n) = \frac{1}{2}[1-\cos(\frac{2n}{N}\pi)]; 0 \le n \le N \quad (12)$$

2.4. SAR image quality metrics

Several measures are used to evaluate the quality of an image. This paper uses peak to the sidelobe ratio (PSLR), based on the relation in Equation (13). PSLR evaluates the shape of the target's impulse response by calculating the ratio between the maximum intensity peak observed in the side lobes and the maximum peak of the corresponding target (Massonnet, Souyris, & Souyris, 2008).

$$PSLR = 20 \times \log(\frac{mainlobe\ power}{peak\ sidelobe\ power}) \quad (13)$$

3. Experiments and Results

Figure 4 shows the imaging geometry of a GB-SAR that operates on a linear rail. In this system, the radar sensor is mounted on a rail and, in every cross-range step, acquires data in a range profile. The developed and implemented radar sensor parameters are based on the designed sensor at the MIT Lincoln laboratory (Charvat, 2014). These parameters are shown in Table 1, where the radar system operates at 2.26 GHz (S-band) carrier frequency and 330 MHz bandwidth, and the aperture length is 1.4 m. In the end, the recorded and prepared raw signal is focused by using the time-domain back-projection algorithm.

The signal acquisition and recording system were implemented in NI LabVIEW[3]. Besides, the signal processing scheme, including the rearranging and preparing the recorded echoes and SAR imaging algorithm were implemented in MATLAB[4] (Hosseiny, Amini, Esmaeilzade, & Nekoee, 2019).

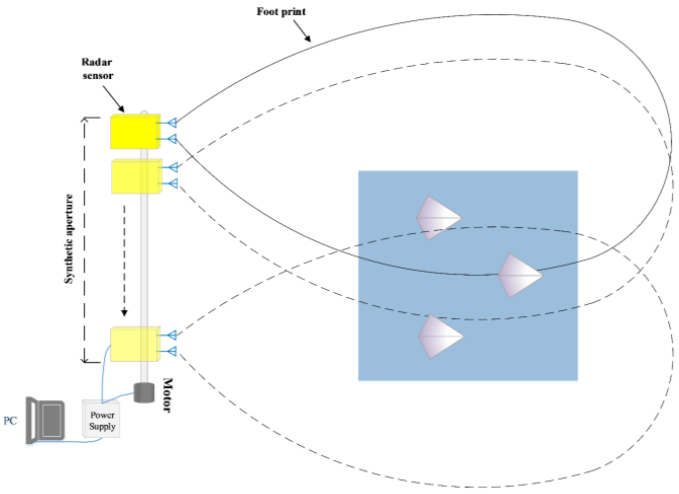

Figure 4. GBSAR imaging geometry

[3] ni.com

[4] mathworks.com

Table 1. Characteristics of the GBSAR

Parameter	Value
Signal type	FMCW
Carrier frequency (f_c)	2.260 GHz (S-band)
Bandwidth (B)	330 MHz
Beat signal bandwidth (B_b)	15 kHz
Sweep time (τ)	20 ms
Sampling frequency (f_s)	44100 Hz
Cross-range steps	1 cm
Aperture length	140 cm
Cross-range steps(N)	140
Range resolution (ρ_r)	0.4545 m
Cross-range resolution (ρ_{cr})	0.0442 rad
Average power (P_{av})	0.001 W
Receiver and transmitter antenna gain ($G_{tx} = G_{rx}$)	7.2 dB
Receiver noise figure (F_n)	1.2 dB
$(SNR)_1$	13.4 dB
System loss (L_s)	6 dB

3.1. Sensor's maximum range

The maximum detectable range of a radar system for a target with a specific RCS value of σ can be calculated based on the radar equation (Equation (7)). The RCS of a flat-plate-shaped corner reflector with the surface of A can be calculated by Equation (14).

$$\sigma = \frac{4\pi A^2}{\lambda^2} \quad (14)$$

Therefore according to Equation (14), for instance, the RCS of square plates with a side of 15 cm or 40 cm are $0.41\ m^2$ (-3.81 dB) or $21.02\ m^2$ (13.23 dB), respectively. Based on the calculated RCS values, the maximum range that radar can detect these targets is 720.19 m or 1920.5 m (based on sensor parameters of Table 1 and Equation (7)), respectively, for a 15 cm and 40 cm square reflector.

However, in the experimental case, the maximum detected range of a radar sensor is limited to the output bandwidth of the beat signal (B_b). Therefore, the maximum detectable range can be calculated by replacing f_b=B_b in Equation (6) and the maximum range can be estimated as: $R_{\max} = \frac{cB_b}{2c_r} = 143.08\,m$. Based on the estimated maximum range of the radar sensor, the minimum detectable target RCS is $6.48\times10^{-4}\,m^2$ or $-31dB$, which can be calculated by inverting Equation (7). The utilized target in this study is a $15^{cm}\times15^{cm}$ square-plate corner-reflector with the RCS of $0.41\ m^2$ or $-3.81dB$, which is higher than the minimum detectable target RCS with the developed sensor.

3.2. Simulation results

At first, the developed GBSAR is evaluated by numerical simulation, where the simulation parameters are shown in Table 1.

Figure 5 shows some impulse responses of point targets located at different slant ranges up to the maximum detectable range. It can be observed that the same point targets are detected wider by increasing their slant-range location. This is because of the limited size of the synthetic aperture in GBSAR systems, where the cross-range resolution depends on the target's slant range (Equation (7)). This issue is evaluated in detail in the subsequent experiments.

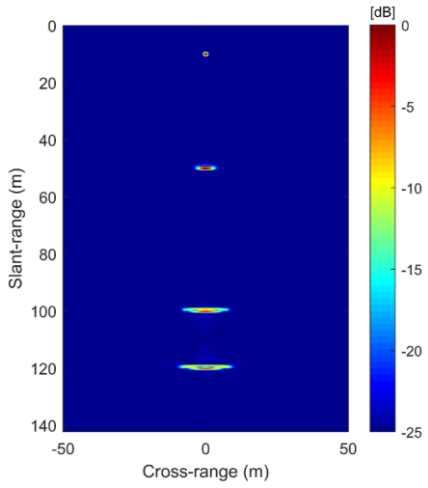

Figure 5. Simulated focused image of implemented GBSAR for point targets at different slant ranges up to the maximum range

In the first simulation, the effects of the signal bandwidth on the range signal are investigated. Table 2 shows the investigated signal bandwidth values and their corresponding theoretical range resolution values, calculated based on Equation (1). Figure 6 shows the range profiles of the four different signals with different bandwidths. Also, four different separations are considered between two-point targets. We can observe that when the separation is 25 cm (Figure 6 a), only the signal with 1 GHz of bandwidth can separate the two-point targets, and, in other bandwidth cases, both targets are merged. When the separation is increased, we can see that targets start to separate in lower bandwidth cases (Figure 6 b). By increasing the targets' separation to 80 cm (Figure 6 c), we can observe that both point targets are separated when using a bandwidth of 200 MHz or 330 MHz; but we can see that the signal with higher bandwidth provides a thinner

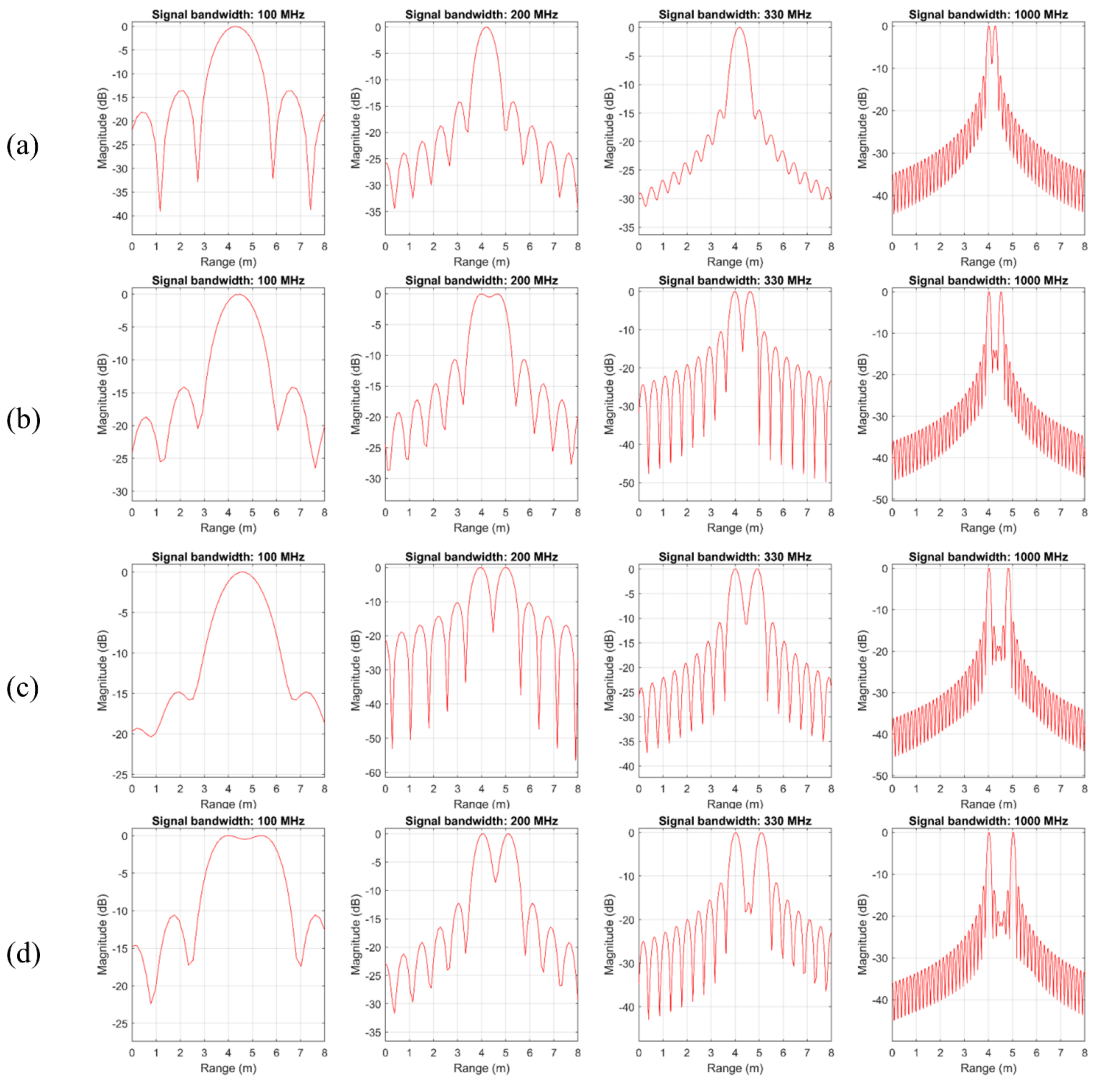

Figure 6. Range profile of four bandwidth cases with two point-target separation of (a) 25 cm (b) 50 cm (c) 80 cm (d) 100 cm

target main lobe and higher PSLR value that is resulted in better signal compression and resolution. In the last case, when the targets' separation is 100 cm (Figure 6 – d), we can see two clear peaks in our three higher signal bandwidths. Even though, in this case, the 100 MHz bandwidth signal has resulted in two peaks, it is still difficult to separate the targets because of lower resolution.

Table 2. Investigated signal bandwidths on range compression resolution

Chirp duration (ms)	Bandwidth (MHz)	Theoretical resolution (m)
20	100	1.50
20	200	0.75
20	330	0.45
20	1000	0.15

In the GBSAR scenario, because of the high variation of scene range compared to synthetic aperture length, cross range resolution is decreasing by maximizing the distance from the sensor (Equation (11)). Therefore, we investigated the cross-range resolution variation of the implemented GBSAR for different slant ranges in the simulated environment in another experiment. Similar to the previous experiment, we consider two point targets, where the cross range distance between them is 100 cm. Table 3 shows the investigated slant-range values and their corresponding theoretical cross-range resolution values, calculated based on Equation (11). Figure 7 shows the cross range profiles of the compressed signals in different slant ranges. We can observe that when the targets are located at three or nine meters away from GBSAR, they can be separated perfectly with two signal peaks, which are clear and thin. However, by increasing the targets' range, the impulse responses became wider, where targets at 21 m were merged and cannot be separated because of the decreasing of cross-

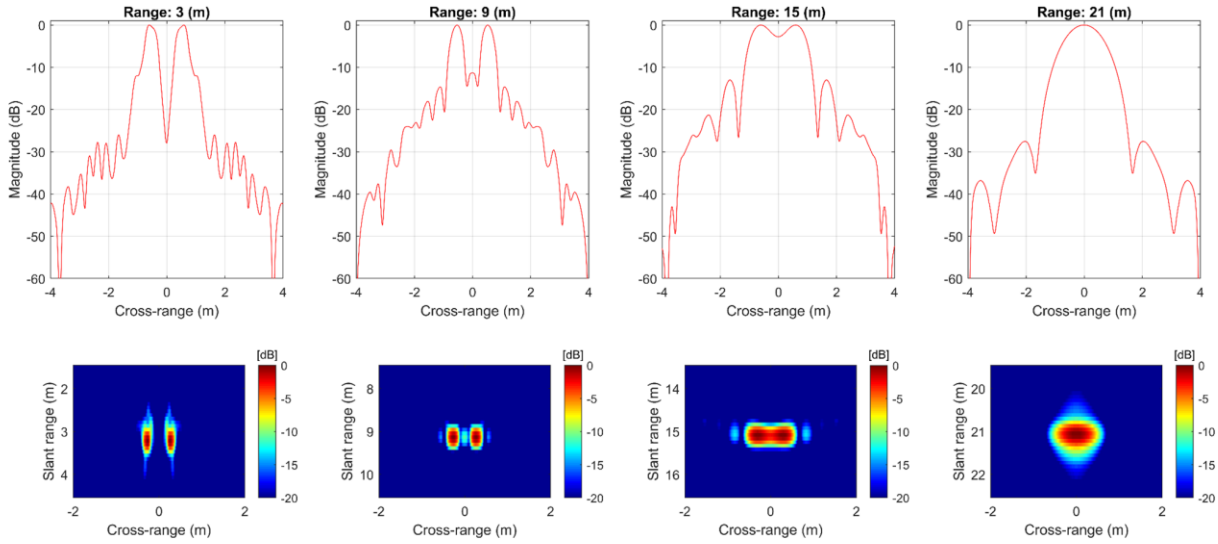

(a) (b) (c) (d)

Figure 7. Cross-range resolution variations in the simulated environment. Targets are located at slant-range of (a) 3 m (b) 9 m (c) 15 m (d) 21 m

range resolution. We can still see two peaks when the targets are located 15 meters away from the GBSAR; however, in this case, cross-range resolution is not high enough to separate the two targets ideally, and some part of the target signals are merged.

Table 3. Investigated different slant-ranges for cross-range resolution

Range (m)	Theoretical cross-range resolution (m)
3	0.1326
9	0.3978
15	0.6630
21	0.9282

In another simulation experiment, we evaluate the effects of the Hann window on the final focused SAR image. Hann window is implemented on the recorded echo. Figure 8 Shows the slant-range and cross-range profiles of four-point targets in the simulated environment before and after implementing the Hann window. Also, Table 4 shows the quantitative results, including slant-and cross-range resolutions and PSLR values. We can observe that by implementing the Hann window on raw data, the main peaks in the focused image contain lower sidelobes in both slant- and cross-range directions. For instance, for a target located at three meters, the slant- and cross-range PSLR values respectively are 15.92 dB and 28.15 dB, while after implementing the Hann window on raw data, the PSLR values are increased to 35.05 dB and 57.59 dB in a slant- and cross-range directions, respectively. We can observe this property in the other three examined cases for targets located at 9, 15, and 21 meters away from the GBSAR sensor. However, it can be seen that implementing the Hann window has made the target peaks in both slant- and cross-range directions thicker than usual, which means losing the resolution. For example, for a target located at three meters, the slant- and cross-range resolutions are 0.493 m and 0.858 m, respectively. However, after implementing the Hann

Table 4. Evaluating the Hann window effect on focused-image in the simulated environment

Targets Range (m)		Slant-range resolution (m)	Cross-range resolution (m)	Slant-range PSLR (dB)	Cross-range PSLR (dB)
3:	Before windowing	0.496	0.272	15.92	28.15
	After windowing	0.707	0.258	35.05	57.59
9:	Before windowing	0.390	0.375	20.93	13.64
	After windowing	0.620	0.601	30.53	35.05
15:	Before windowing	0.376	0.623	23.19	14.58
	After windowing	0.613	0.975	30.35	36.16
21:	Before windowing	0.493	0.858	23.67	15.29
	After windowing	0.701	1.324	35.59	40.00

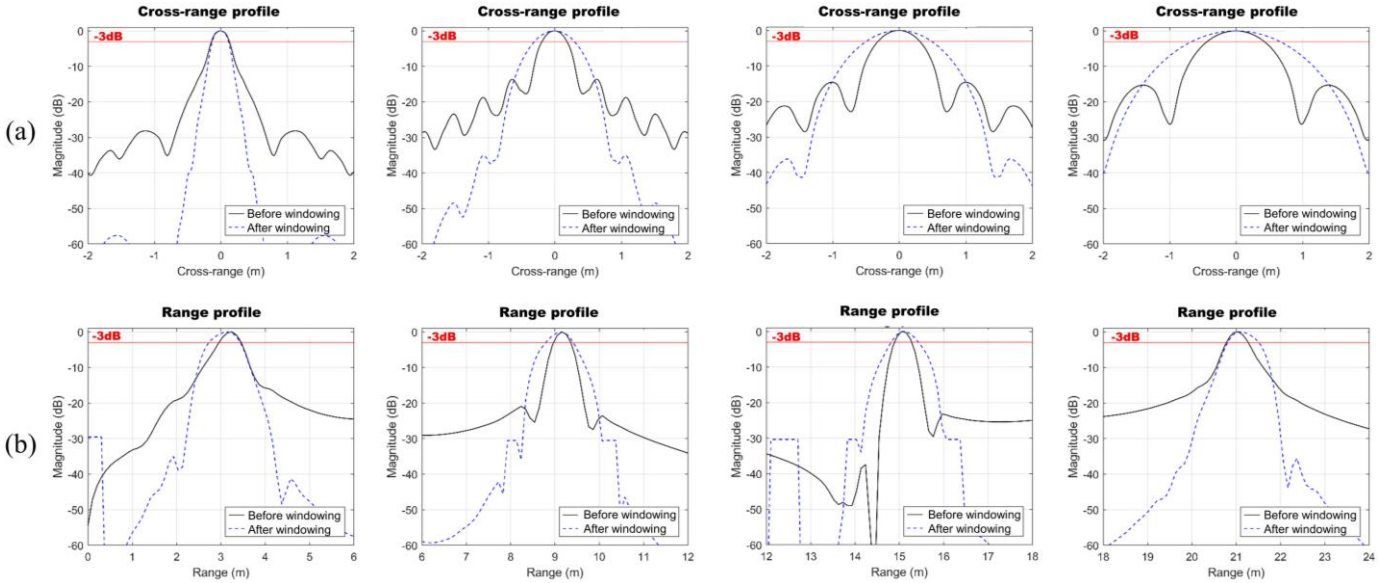

Figure 8. Comparison of impulse responses before and after implementing Hann window for (a) Cross-range direction (b) Slant-range direction

window on raw signal, the resolutions were altered to 0.701 m and 1.324 m in a slant- and cross-range directions, respectively, which means we have lost resolution after Hann windowing.

3.3. Experimental results

Three different experiments were conducted, including an experiment with one corner reflector in the center of the scene and two experiments with two corner reflectors with different positioning in the imaging scene. All the experiments were conducted in the slant range of fewer than two meters because of the system's low power and lab area limits. We used 15 cm^2 plate corner reflectors as reflecting targets in the imaging scene.

Figure 9 visually compares the focused images of the three conducted experiments with their simulations' results. Simulated targets are assumed as ideal point targets in the imaging scene. The peak areas of each target are taken to calculate the quality metrics. The focusing performance results of the back-projection algorithm are shown in Table 5. Regarding the acquired results, the corner reflector's slant range and cross-range resolution located at R = 1.5 are 0.4522 m and 0.1193 m, respectively. In comparison, the acquired results for simulating the same scene are slant range resolution of 0.4512 m and cross-range resolution of 0.0820 m.

Accordingly, both experimental and simulation results are slightly weaker than the theoretical calculations of the range and cross-range resolutions. Regarding the acquired PSLR values, experimental results obtained close results compared to the simulations, which indicates the good performance of the radar sensor on receiving the backscattered echo and focusing capability of the developed SAR sensor using the back-projection algorithm.

Table 5. Focusing performance of the BP algorithm, implemented on the GBSAR data

R = 1.5 m	Slant-range resolution (m)	Cross-range resolution (m)	Slant-range PSLR (dB)	Cross-range PSLR (dB)
Experiment	0.4522	0.1193	23.59	13.02
Simulation	0.4512	0.0820	24.42	15.33
Theoretical	0.4027	0.0663		

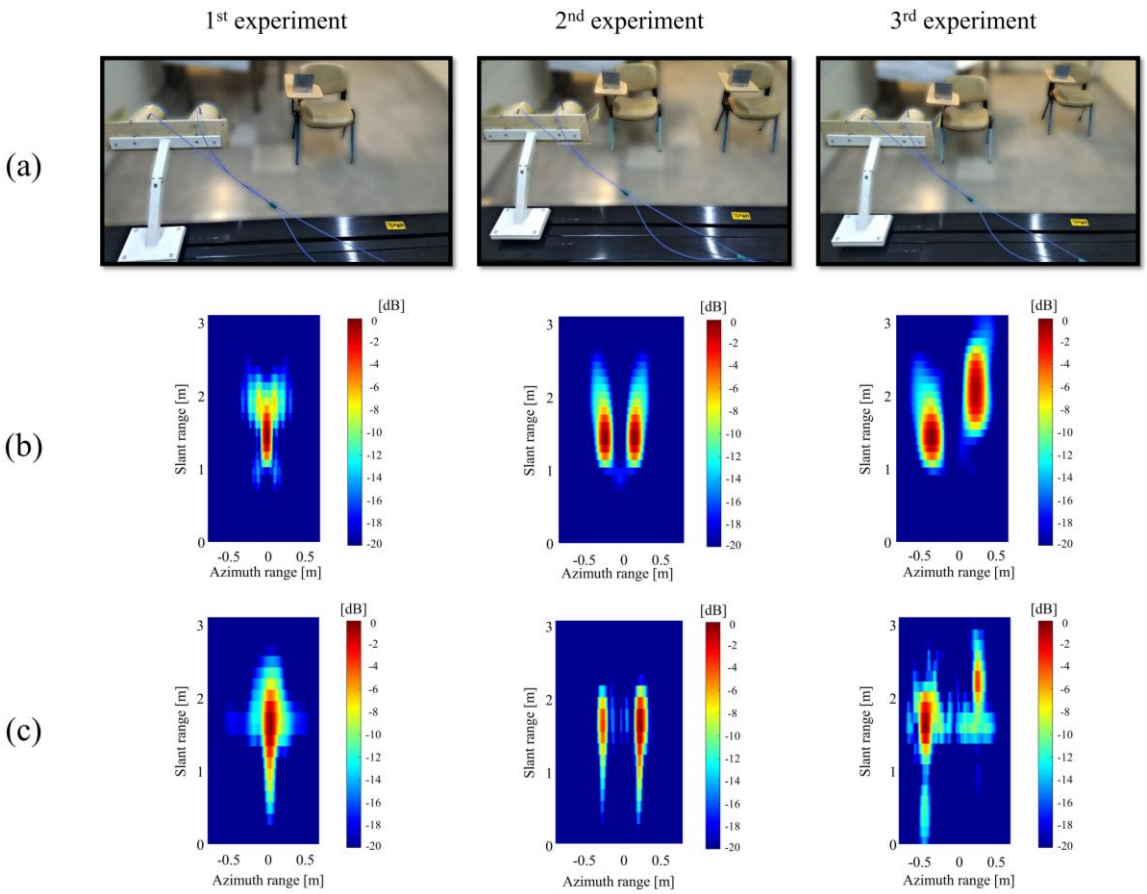

Figure 9. Comparing the visual results of the laboratory experiments with simulated results. (a) Imaging scene (b) Simulated (c) Real data

Hann window was implemented on the raw signal in order to improve the quality of the raw signal and the resulting SAR image. Figure 10 shows the effect of the implementation of the Hann window on a single received dechirped signal. Hann window, as a weighting function, suppresses the less frequent signal samples.

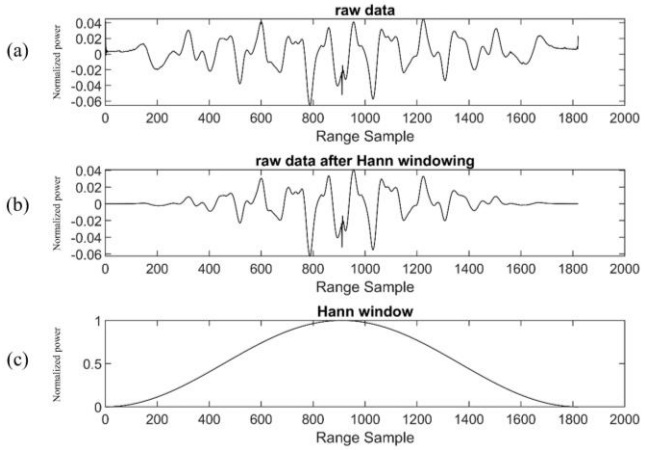

Figure 10. Hann windowing effect on a raw signal: (a) raw signal before Hann windowing (b) raw signal after Hann windowing (c) Hann window

Figure 11 visually compares the Hann windowing effects on the focused images of the conducted experiments. The quantitative comparison of focused image quality before and after implementing the Hann window has been provided in Table 6. Regarding the results, in most cases, PSLR values are increased, which means the suppression of targets' sidelobes and increasing the quality of the target focusing after Hann windowing. However, by comparing the obtained results in Table 6 with simulation results in Table 4 shows that the Hann window had lower effects on our sensor's data. Overall, by observing the visual results in Figure 11 and quantitative results in Table 6 shows that Hann windowing was able to increase the quality of the focused image of the SAR sensor; however, in some cases, there is a loss in cross-range resolution.

4. Conclusion

In this paper, we presented the signal processing experiments to evaluate the developed GBSAR at MRESL of the University of Tehran. The designed sensor consists of an S band radar sensor that is mounted on a 1.4 m rail with a stepper motor. The radar sensor moves every 1 cm and acquires the radar backscatters. At each step of the radar sensor, the backscattered echo is recorded. After signal preparation and pre processing steps, the signal becomes

Table 6. Evaluating the Hann windowing effect on conducted experiments

	Experiment ID	Slant-range resolution (m)	Cross-range resolution (m)	Slant-range PSLR (dB)	Cross-range PSLR (dB)
1	Before windowing	0.4522	0.1245	22.51	12.89
	After windowing	0.4522	0.1193	23.59	13.02
2	Before windowing	0.4253	0.1320	22.65	13.34
	After windowing	0.4253	0.1271	21.30	12.97
3	Before windowing	0.3906	0.0994	12.66	11.72
	After windowing	0.3776	0.1073	17.56	12.35

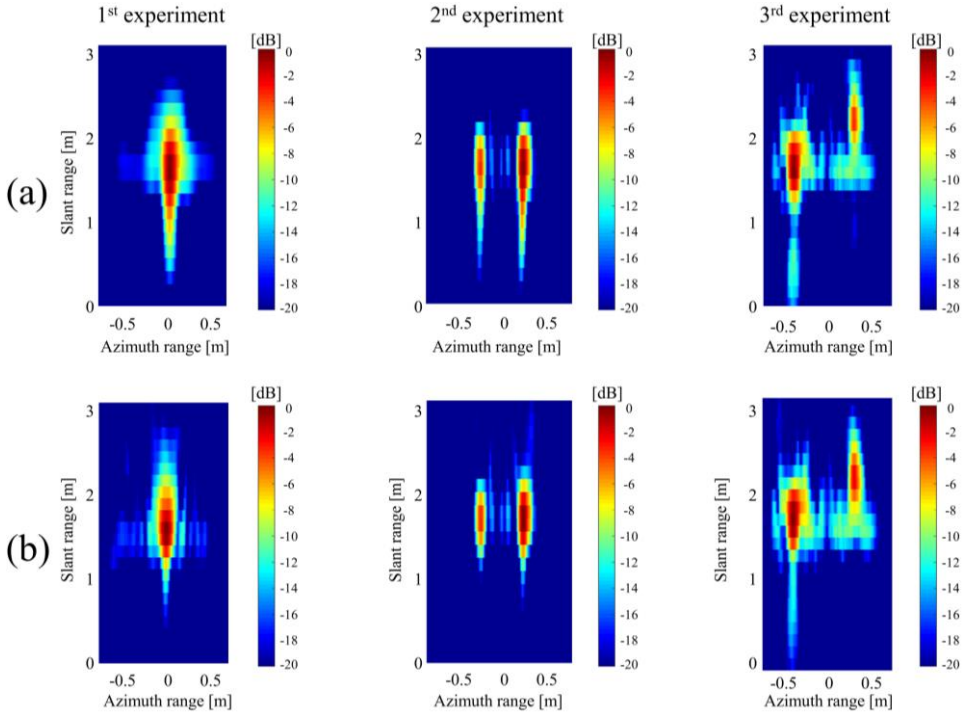

Figure 11. Experiments: (a) before Hann windowing (b) after Hann windowing

ready to be fed to a SAR processing algorithm. Finally, the focused SAR image is generated by slant range and cross-range compression of the raw data by implementing the time-domain back-projection algorithm. In order to evaluate the capabilities and applicability of the developed system, several experiments were conducted based on numerical simulations and laboratory tests. Accordingly, target detection and separation capabilities were evaluated by numerical simulations. Furthermore, three different laboratory experiments using 15 cm^2 rectangular corner reflectors were conducted. The experimental results were validated and evaluated by comparing the slant range and cross-range resolutions and PSLR values with the numerical simulation. In order to improve the focusing results, Hann windowing was implemented on the raw signals. As the Hann window works as a smoothing function by suppressing the weak signals, it caused to slight resolution reduction in both range and cross-range directions. However, applying the Hann window on simulated or real signals resulted in significant improvements in targets' impulse response signal in range and cross-range directions.

References

Alba, M., Bernardini, G., Giussani, A., Ricci, P. P., Roncoroni, F., Scaioni, M., … others. (2008). Measurement of dam deformations by terrestrial interferometric techniques. *The International Archives of the Photogrammetry, Remote Sensing and Spatial Information Sciences*, *37*(1374), 133–139.

Anghel, A., Tudose, M., Cacoveanu, R., Datcu, M., Nico, G., Masci, O., … Ding, Z. (2019). Compact ground-based interferometric synthetic aperture radar: Short-range structural monitoring. *IEEE Signal Processing Magazine*, *36*(4), 42–52.

Bamler, R., & Hartl, P. (1998). Synthetic aperture radar interferometry. *Inverse Problems*, *14*(4), R1.

Bernardini, G., Ricci, P., Coppi, F., & others. (2007). A ground based microwave interferometer with imaging capabilities for remote measurements of displacements. *Proc. 7th Geomatic Week*.

Brooker, G. (2011). *Introduction to sensors for ranging and imaging*. The Institution of Engineering and Technology. https://doi.org/10.1017/CBO9781107415324.004

Carrara, W. G., Goodman, R. S., & Majewski, R. M. (1995). *Spotlight synthetic aperture radar : signal processing*

algorithms. Boston : Artech House. Retrieved from https://searchworks.stanford.edu/view/3116166

Casagli, N., Catani, F., Del Ventisette, C., & Luzi, G. (2010). Monitoring, prediction, and early warning using ground-based radar interferometry. *Landslides*, *7*(3), 291–301. https://doi.org/10.1007/s10346-010-0215-y

Charvat, G. L. (2014). *Small and short-range radar systems*. CRC Press.

Dammann, D. O., Johnson, M. A., Fedders, E. R., Mahoney, A. R., Werner, C. L., Polashenski, C. M., … Hutchings, J. K. (2020). Ground-Based Radar Interferometry of Sea Ice. *Remote Sensing 2021, Vol. 13, Page 43*, *13*(1), 43. https://doi.org/10.3390/RS13010043

Del Ventisette, C., Intrieri, E., Luzi, G., Casagli, N., Fanti, R., Leva, D., … Keefer, D. (2011). Using ground based radar interferometry during emergency: the case of the A3 motorway (Calabria Region, Italy) threatened by a landslide. *Natural Hazards & Earth System Sciences*, *11*(9).

Hanssen, R. F. (2001). *Radar interferometry: data interpretation and error analysis* (Vol. 2). Springer Science & Business Media.

Heinzel, G., Rüdiger, A., & Schilling, R. (2002). Spectrum and spectral density estimation by the Discrete Fourier transform (DFT), including a comprehensive list of window functions and some new at-top windows.

Hosseiny, B., & Amini, J. (2018). Evaluation of a Signal Processing Algorithm in a Ground-Based SAR System in Simulated Environment. *ISSGE*, *8*(2), 189–198. Retrieved from http://jgst.issge.ir/article-1-723-en.html

Hosseiny, B., Amini, J., Esmaeilzade, M., & Nekoee, M. (2019). Range Migration Algorithm in the Processing Chain of Signals of a Ground-Based SAR Sensor. *The International Archives of Photogrammetry, Remote Sensing and Spatial Information Sciences*, *42*, 521–525.

Komarov, I. V, & Smolskiy, S. M. (2003). *Fundamentals of short-range FM radar*. Artech House.

Li, C., Peng, Z., Huang, T.-Y., Fan, T., Wang, F.-K., Horng, T.-S., … Lin, J. (2017). A review on recent progress of portable short-range noncontact microwave radar systems. *IEEE Transactions on Microwave Theory and Techniques*, *65*(5), 1692–1706.

Luo, Y., Song, H., Wang, R., Deng, Y., Zhao, F., & Xu, Z. (2014). Arc FMCW SAR and applications in ground monitoring. *IEEE Transactions on Geoscience and Remote Sensing*, *52*(9), 5989–5998.

Martinez-Vazquez, A., & Fortuny-Guasch, J. (2007). Snow avalanche detection and classification algorithm for GB-SAR imagery. In *Geoscience and Remote Sensing Symposium, 2007. IGARSS 2007. IEEE International* (pp. 3740–3743).

Massonnet, D., & Feigl, K. L. (1998). Radar interferometry and its application to changes in the Earth's surface. *Reviews of Geophysics*, *36*(4), 441–500.

Massonnet, D., Souyris, J.-C., & Souyris, J.-C. (2008). *Synthetic Aperture Radar Imaging*. EFPL Press. https://doi.org/10.1201/9781439808139

Meta, A., Hoogeboom, P., & Ligthart, L. P. (2007). Signal processing for FMCW SAR. *IEEE Transactions on Geoscience and Remote Sensing*, *45*(11), 3519–3532.

Oppenheim, A. V. (1999). *Discrete-time signal processing*. Pearson Education India.

Penner, J. F., & Long, D. G. (2017). Ground-based 3D radar imaging of trees using a 2D synthetic aperture. *Electronics*, *6*(1), 11.

Pieraccini, M. (2013). Monitoring of civil infrastructures by interferometric radar: A review. *The Scientific World Journal*, *2013*.

Pieraccini, M., & Miccinesi, L. (2019). An interferometric MIMO radar for bridge monitoring. *IEEE Geoscience and Remote Sensing Letters*, *16*(9), 1383–1387.

Podder, P., Khan, T. Z., Khan, M. H., & Rahman, M. M. (2014). Comparative Performance Analysis of Hamming, Hanning and Blackman Window. *International Journal of Computer Applications*, *96*(18), 975–8887. Retrieved from http://citeseerx.ist.psu.edu/viewdoc/download?doi=10.1.1.681.6082&rep=rep1&type=pdf

Richards, M. A., Scheer, J., Holm, W. A., & Melvin, W. L. (2010). *Principles of modern radar*. Citeseer.

Schaffhauser, A., Adams, M., Fromm, R., Jörg, P., Luzi, G., Noferini, L., & Sailer, R. (2008). Remote sensing based retrieval of snow cover properties. *Cold Regions Science and Technology*, *54*(3), 164–175.

Skolnik, M. I. (Merrill I. (2003). *Introduction to radar systems*. McGraw Hill.

Soumekh, M. (1999). *Synthetic aperture radar signal processing* (Vol. 7). New York: Wiley.

Tarchi, D., Rudolf, H., Luzi, G., Chiarantini, L., Coppo, P., & Sieber, A. J. (1999). SAR interferometry for structural changes detection: a demonstration test on a dam. In *International Geoscience and Remote Sensing Symposium (IGARSS)* (Vol. 3, pp. 1522–1524). IEEE. https://doi.org/10.1109/igarss.1999.772006

Ting, J.-W., Oloumi, D., & Rambabu, K. (2017). FMCW SAR System for Near-Distance Imaging Applications--Practical Considerations and Calibrations. *IEEE Transactions on Microwave Theory and Techniques*.

Ulaby, F., Long, D., Blackwell, W., Elachi, C., Fung, A., Ruf, C., … Van Zyl, J. (2014). *Microwave radar and radiometric remote sensing*. Ann Arbor: University of Michigan Press. Retrieved from http://titlealert.alkemlibrary.com/attachments/546/Artech House ABI - Mar 15 - Ulaby.pdf

Yang, R., Li, H., Li, S., Zhang, P., Tan, L., Gao, X., & Kang, X. (2018). *High-Resolution Microwave Imaging*. Springer.

Zaugg, E. C., & Long, D. G. (2015). Generalized frequency scaling and backprojection for LFM-CW SAR processing. *IEEE Transactions on Geoscience and Remote Sensing*, *53*(7), 3600–3614.